Petroleum Science 22 (2025) 4504–4519

Contents lists available at ScienceDirect

Petroleum Science

journal homepage: www.keaipublishing.com/en/journals/petroleum-science

Original Paper

Near-wellbore 3D velocity imaging inversion method based on array acoustic logging data

Zi Wang [a], Wen-Zheng Yue [a,*], Yu-Ming Zhu [a], Nai-Xuan Ji [b], Shan-Shan Fan [a]

[a] State Key Laboratory of Petroleum Resources and Engineering, China University of Petroleum (Beijing), Beijing, 102249, China
[b] School of Earth Sciences, Yunnan University, Kunming, 650091, Yunnan, China

ARTICLE INFO

Article history:
Received 5 March 2025
Received in revised form
3 April 2025
Accepted 30 June 2025
Available online 4 July 2025

Edited by Meng-Jiao Zhou

Keywords:
Acoustic logging
Radial profile
Velocity inversion
Azimuthal velocity

ABSTRACT

The characterization of subsurface formations via the analysis of near-wellbore velocity profiles represents a crucial method in geophysical exploration. This technique enables the evaluation of key parameters, including rock brittleness, wellbore stability, fracturing effects, and invasion extent, thereby enhancing comprehension of formation structures and informing exploration strategies. However, traditional near-wellbore formation velocity imaging methods exhibit two principal limitations. First, these methods lack azimuthal sensitivity, yielding results averaged across all directions. Second, they are computationally intensive and impractical for well-site environments. To address these drawbacks, we developed a rapid 3D velocity imaging method for array acoustic logging instruments equipped with azimuthal receivers, capable of producing 3D imaging results efficiently. The workflow entails the following steps: (1) Band-pass filtering of logging data to mitigate scattered wave interference caused by formation heterogeneity near the wellbore; (2) combination of receivers with varying detection ranges in each direction to derive radial velocity sequences, followed by integration of ray-tracing theory to obtain 2D velocity distributions; and (3) synthesis of final 3D velocity imaging results via interpolation of these 2D datasets. In the velocity sequence extraction process, we significantly reduced the computational load by employing an adaptive time window, ensuring rapid and stable application in well-site settings. We utilized the finite difference method to construct well models with heterogeneous formations. The compressional and shear wave 3D velocity imaging results derived from synthetic data correlated with the model, demonstrating the azimuthal sensitivity of our proposed method. Furthermore, we applied this method to a well in West China, successfully identifying the azimuth of near-wellbore anisotropy.

1. Introduction

Compressional and shear wave velocities are important petrophysical properties as they are closely related to formation lithology (Bourbié et al., 1992). The properties of the near-wellbore formation are often impacted by mechanical damage and fluid intrusion during drilling (Baker and Winbow, 1988). Well-completion can also cause microfractures in the near-wellbore formation. These different situations can cause velocity variations in formation (Pistre et al., 2005). Accordingly, the distribution of the velocity is of great importance for assessing borehole stability (Winkler, 2005), estimating formation stress (Sayers et al., 2008), optimizing reservoir production (Tang et al., 2016,b), and guiding well drilling completion (Sinha et al., 2005). Although array acoustic logging is an effective method for measuring velocity variations along the axial direction of the borehole, the radial velocity information cannot be quantitatively obtained from the conventional waveform semblance analysis (Willis and Toksöz, 1983; Kimball and Marzetta, 1984).

To this end, several methods have been proposed to perform the inversion of the radial velocity. Hornby (1997) devised a tomographic reconstruction method using the simultaneous iterative reconstruction technique (SIRT) (Dines and Lytle, 1979) and the ray-tracing theory, showing the potential for ray-tracing tomography to obtain the radial velocity variations around a

* Corresponding author.
E-mail address: yuejack1@sina.com (W.-Z. Yue).
Peer review under the responsibility of China University of Petroleum (Beijing).

https://doi.org/10.1016/j.petsci.2025.06.023

borehole. On this basis, Zeroug et al. (2006) proposed an inversion method based on an improved first motion algorithm (Valero et al., 2004) and ray-tracing theory, making the method fast, robust, and suitable for the well-site environment. However, the inversion based on travel time has high requirements for estimating refracted wave first arrival times (Sinha, 2004). To solve the dependency on refracted wave first arrival times, Liu et al. (2021) developed a stepwise inversion method mitigating inaccuracies in processing field data with noises. Sinha et al. (2006) proposed to use the technique based on the Backus-Gilbert theory (Backus et al., 1970) in the inversion of the measured cross-dipole dispersions to map the average velocity distribution at the expense of radial resolution, which is applicable for both increasing and decreasing velocity profiles. Tang et al. (2016b) adopted a new constraint to solve the non-unique problem of estimating the radial variation from dispersion data. Moreover, Ma et al. (2013) used the perturbation method and Backus-Gilbert theory to map the radial alteration of formation shear wave velocity, which proved that the method has good noise resistance. Tang et al. (2023) applied the full-waveform inversion (FWI) (Tarantola, 1984) technique to wireline monopole acoustic logging data to image the near-wellbore formation velocity structures. Wang and Yue (2024) were focusing on the velocity imaging in thin beds due to the inability of array acoustic logging to accurately characterize the properties of thin beds, and have made significant progress in this area. However, these methods can only provide a 2D (axial and radial) velocity profile and fail to determine the main direction contributed to the radial velocity variation.

To solve the azimuthal sensitivity limitation of the radial velocity inversion method, we propose a fast 3D velocity imaging method for array acoustic logging instruments with azimuthal receivers, which can obtain near-wellbore 3D velocity imaging results quickly and efficiently. In the new method, we first use frequency domain methods to process the array acoustic logging data to determine the appropriate frequency range for subsequent bandpass filtering, in order to retain the true azimuthal refracted compression wave and refracted shear wave. This step aims to reduce the scattered wave interference caused by the formation heterogeneity and ensure that the signals from azimuthal receivers can reflect the formation information in its corresponding direction. Next, the receiver array in each direction is regrouped, starting with the receiver with the shortest source distance. The first receiver and the next few receivers form the first group, the second receiver and the next few receivers form the second group, and so on, until the receiver with the maximum source distance is placed in the last group. This step aims to utilize the characteristic of the array acoustic logging tool that the radial detection depth increases with the source distance to obtain formation velocity information at different detection ranges. Then, the slowness (reciprocal of velocity) time coherence (STC) method (Kimball and Marzetta, 1984) with an adaptive time window is used to calculate the velocity of the grouped signals so that a velocity sequence varying with the number of groups is obtained. The purpose of the adaptive time window is to improve the efficiency by reducing the unnecessary computational areas. By combining the velocity sequence with the ray tracing theory, the radial depth corresponding to the velocity can be obtained, as well as the two-dimensional velocity profile in this direction. Finally, based on the 2D velocity profiles in each direction, the inverse-distance weighting (IDW) interpolation method is employed to build the near-wellbore 3D velocity distribution image. The technical route of the proposed method is shown in Fig. 1. We apply this method to deal with the field data and the synthetic data obtained by the finite difference method in time domain (FDTD) (Cheng et al., 1995). The inversion results of the synthetic and field examples verify the accuracy and performance of the proposed method.

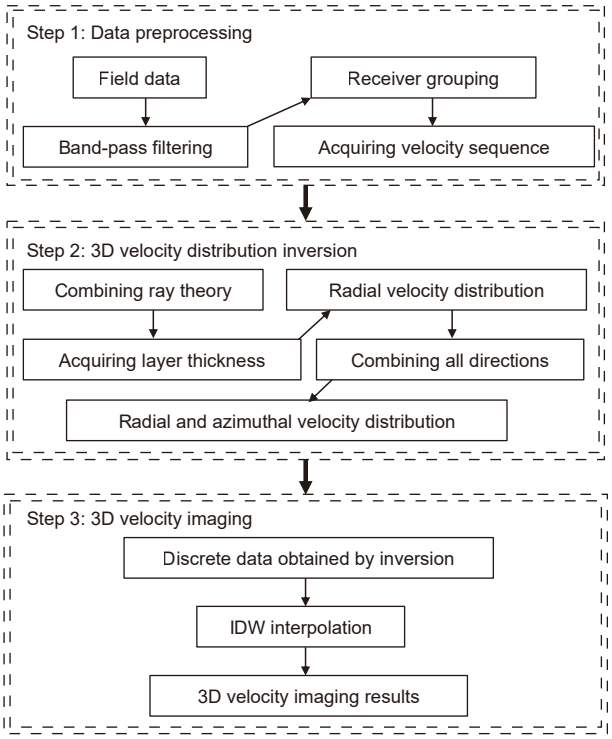

Fig. 1. Near-wellbore 3D velocity imaging work flow.

2. Methodology

2.1. Waveform acquisition and merging

In our study, the design of data acquisition system in the simulation follows the configuration of modern acoustic logging tool, the Xaminer Sonic Imager™ (Walker et al., 2015). As illustrated in Fig. 2, the logging tool contains 13 equally spaced receiver rings of 0.1524 m (0.5 ft) spacing and four monopole sources located at different positions. Each receiver ring can be viewed as a combination of 8 receivers spaced 45° apart. We only model the lower-near monopole and far monopole in the simulations. These two monopole sources are excited separately at each logging depth to generate two independent data sets. This method is not instrument-specific and can be applied to data from Schlumberger's Sonic Scanner and Baker Hughes' XMAC-II, both of which utilize a combined far- and near-monopole excitation mode with azimuthal receiver arrays.

The numerical simulations follow the working pattern of field data acquisition: the tool logs every 0.1524 m along the borehole axis. All monopole sources will use the Ricker wavelet $S(t)$ with centre frequencies f_0 of 10 kHz, which aligns with the monopole mode frequencies of Halliburton's Xaminer Sonic Imager. In balancing the demands of detection range and detection accuracy, the commonly used excitation frequency range for monopole acoustic logging is 8–12 kHz, and the method we propose is applicable to any excitation frequency within this range. The source function is written as:

$$S(t) = \left(1 - 2(\pi f_0(t - t_0))^2\right) e^{-(\pi f_0(t-t_0))^2} \quad (1)$$

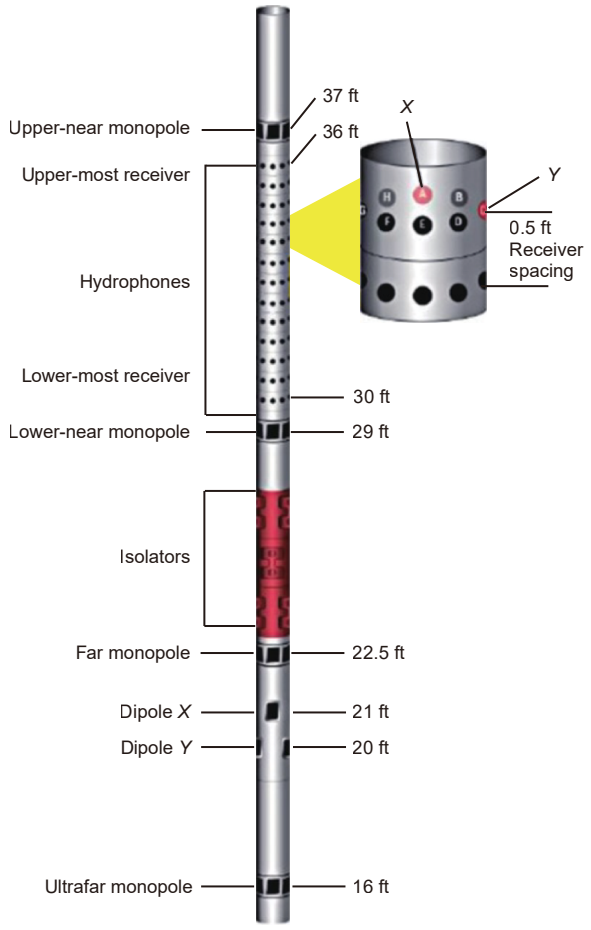

Fig. 2. Schematic of the Halliburton Xaminer Sonic Imager™ (Walker et al., 2015).

where t_0 represents the delay time, which has the following relationship with f_0:

$$t_0 = \frac{1.5}{f_0} \tag{2}$$

As shown in Fig. 3, the two monopole sources at different distances from the receivers create data of different offsets. We can consolidate the data acquired at the same source depths and create shot gathers that contain 26 equally spaced receivers with offsets ranging from 0.3048 to 4.1148 m (1–13.5 ft). Our near-wellbore 3D

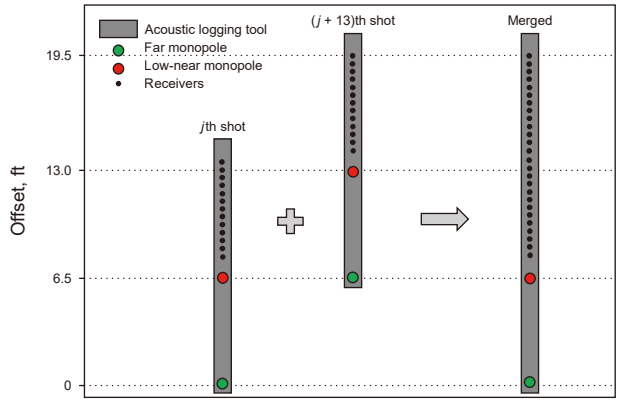

Fig. 3. Schematic representation of the merging of low-near and far monopole waveforms (26 equally spaced receivers with offsets ranging from 1 to 13.5 ft).

velocity imaging workflow is based on the merged monopole data sets to obtain richer velocity information around the well. However, the workflow can also be applied to a data set with only one monopole source. Next, we will detail the theory of azimuthal velocity extraction, radial velocity extraction, and borehole 3D velocity interpolation imaging.

2.2. Determination of the frequency range for azimuthal velocity extraction

Azimuthal velocity extraction with strong heterogeneity remains challenging because scattering can significantly affect wave propagation, resulting in changes in wave travel time, amplitude, waveform, and spectrum (Tang et al., 2016a). Two main characteristics of the scattered waves in the logging scale are the amplitude of scattered waves decreasing with time (Lei et al., 2019) and the main frequency of scattered waves decreasing with time (Schisselé et al., 2004). When the refracted wave propagates at the boundary between the fast and the slow formations, scattered waves tend to be faster than the refracted compression waves of the slow formation. The receiver located in the slow formation will receive the scattered wave signal first, and the refracted and scattered waves are aliased in the time domain, which makes the velocity extraction inaccurate. Therefore, we first utilize the weighted spectral semblance (WSS) method (Nolte et al., 1997) in the conventional frequency-domain velocity analysis to process the array acoustic logging data, which can reveal the frequency-domain distribution characteristics of refracted waves and scattered waves, thereby enabling the assessment of their correlation. Through correlation analysis, it can be observed that the correlation of refracted waves from the direction of the receiving transducer is greater than that of the scattered waves from other directions. This helps us to determine the appropriate frequency domain range as a basis for azimuthal velocity extraction.

2.3. Azimuthal velocity extraction after bandpass filtering

After determining the appropriate frequency range using the WSS method, we first apply bandpass filtering to the dataset to focus the frequency range within the domain of the refracted compressional or refracted shear waves as the predominant mode waves. The advantage of this is that the actual refracted wave signal is preserved while the scattered signal is significantly suppressed. The following filtering principle was applied: Given an expression of merged monopole data sets $W(t)$ in the time domain, the expression $W(e^{j\omega})$ in the frequency domain can be obtained by Fourier transform as:

$$W\left(e^{j\omega}\right) = \int_{-\infty}^{+\infty} W(t)e^{-j\omega t}dt \tag{3}$$

where ω represents the angular frequency. Next, we design a bandpass filter to filter the time domain waveform in the frequency domain:

$$H(j\omega) = \begin{cases} 1, \text{when} & f_1 < f < f_2 \\ 0, \text{when} & f < f_1 \text{ or } f > f_2 \end{cases} \tag{4}$$

where $H(j\omega)$ represents the filter factor, and f_1 and f_2 represent the lower and upper-frequency limits of the filter applicable to the monopole array acoustic logging scale, respectively.

Multiplying $W(e^{j\omega})$ and $H(j\omega)$ and then performing inverse Fourier transform obtains a filtered waveform in the time domain:

$$W_f(t) = \frac{1}{2\pi}\int_{-\pi}^{\pi} W\left(e^{j\omega}\right)H(j\omega)e^{j\omega t}d\omega \tag{5}$$

where $W_f(t)$ represents the time domain waveform obtained after filtering.

We use the STC method to process the filtered waveform of each azimuthal receiver array to obtain 2D similarity coefficient images of time and velocity in each direction. The advantage of the STC method is that it exploits the principle of waveform correlation and does not depend on the arrival time of the refracted wave, which is suitable for the subset of data after band-pass filtering. The similarity coefficient $\rho(s, T)$ of the time-slowness correlation method can be written as:

$$\rho(s,T) = \frac{\int_{T_i}^{(T_i+T_w)}\left|\sum_{m=1}^{N} W_{fm}[t+s(m-1)d]\right|^2 dt}{N\int_{T_i}^{(T_i+T_w)}\sum_{m=1}^{N}\left|W_{fm}[t+s(m-1)d]\right|^2 dt} \tag{6}$$

where s is the slowness value, T_i is the time of recorded data, T_w is the length of the time window, W_{fm} is the filtered waveform received by the mth receiver of the receiver array, d is the receiver spacing, and N is the number of receiver rings.

The refracted wave velocity equals the reciprocal of the slowness value corresponding to the high correlation position. In this way, we preliminarily obtain the velocity distribution of eight directions at a depth point. However, the heterogeneity of the formation is reflected not only in the azimuth velocity difference but also in the radial velocity variation due to drilling damage and drilling fluid intrusion. Next, we will detail the method of determining the radial velocity distribution.

2.4. Determining the radial velocity distribution

Generally, the investigation depth of the array acoustic logging instrument increases with the enlargement of offset distance. When the offset exceeds a certain critical distance, the radial investigation range will not increase further because of the limited energy of the monopole source. The offset distance and investigation depth cannot be directly calibrated because their relationship is not linear. Accordingly, we group the 26 receiver waveforms in each direction. The waveforms of each adjacent four receivers are used as a group, resulting in 23 groups, as shown in Fig. 4. The STC method extracts the velocity separately for each group, and 23 velocity sequences are obtained in one direction. The above process is repeated in other directions to obtain velocity sequences in eight directions at each sampling point. The sequence number can reflect the investigation depth to a certain extent. Although we can qualitatively determine that the velocity presents a near-to-far distribution in the radial direction as the sequence number increases. However, the spacing between two adjacent velocities remains undetermined and cannot constitute a two-dimensional velocity and radial distance profile.

In order to quantitatively characterize the two-dimensional distribution of velocities in each direction, we combine the velocity sequences with ray-tracing theory to obtain the spacing between adjacent velocities. We illustrate this approach using a radial layered model. Fig. 5 shows the transmission paths of refracted waves in this model. It is assumed that the region of velocity variation is divided into n layers in radial; the $(n+1)$th layer is the undisturbed formation. H_1 to H_n represent the thickness of each layer in the region of velocity variation, v_1 to v_n represent their layer velocity, and v_{n+1} is the velocity of the undisturbed formation. The number of receiver rings is N, the receiver spacing is d, and the source distance is z_0. If combining every i ($i = 3, 4, 5$ …) adjacent receiver in the tool as a group, the average source distance z_k of group k is:

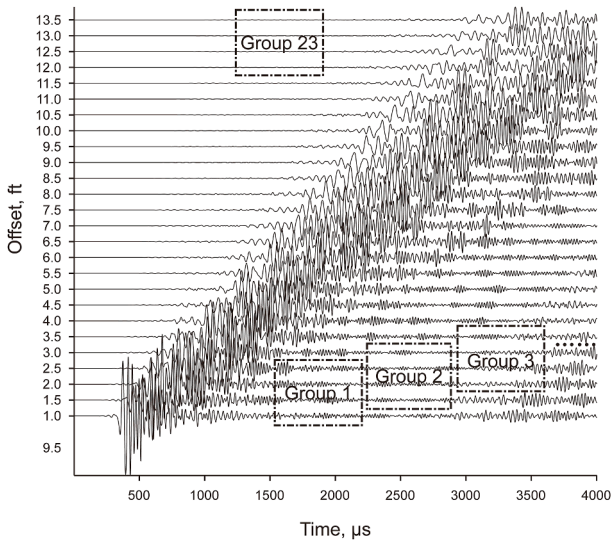

Fig. 4. Schematic of the merged waveform regrouping (A total of 23 groups were formed from the first group until the end).

$$z_k = z_0 + \frac{(i+k-2)d}{2}, \quad k = 1, 2, \cdots, (N-i+1) \tag{7}$$

The overall travel time T_n of refracted compression wave or refracted shear wave travelling within the nth layer is expressed as:

$$T_n = \frac{z_k}{v_{n+1}} + \sum_{i=1}^{n}\frac{2H_i\sqrt{{v_{n+1}}^2 - {v_i}^2}}{v_{n+1}v_i} \tag{8}$$

The time of wave passing through layer H_n is longer than that of

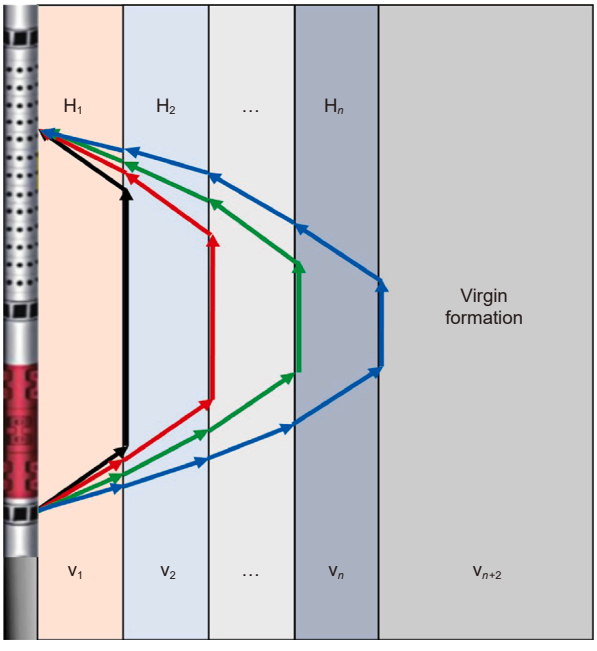

Fig. 5. Transmission paths of refracted wave in radial variation formation.

layer $H_{n\text{-}1}$, therefore, the thickness H_n can be obtained according to Eq. (8):

$$H_n = \frac{\frac{z_k}{v_n} - \frac{z_k}{v_{n+1}} + \sum_{i=1}^{n-1} 2H_i \left(\frac{\sqrt{v_n^2 - v_i^2}}{v_n v_i} - \frac{\sqrt{v_{n+1}^2 - v_i^2}}{v_{n+1} v_i} \right)}{\frac{2\sqrt{v_{n+1}^2 - v_n^2}}{v_n v_{n+1}}}, \quad n = 2, 3, \cdots \tag{9}$$

and the first layer thickness H_1 is expressed as:

$$H_1 = \frac{1}{2} \left(\frac{\frac{z_k}{v_1} - \frac{z_k}{v_2}}{\sqrt{\frac{v_2^2 - v_1^2}{v_1 v_2}}} \right) \tag{10}$$

The radial position corresponding to the velocity sequence can be automatically obtained through Eqs. (9) and (10). We repeat this process for the velocity sequence in each direction to obtain a two-dimensional velocity profile in each direction at a sampling point. With the instrument recording every 0.1524 m along the borehole axis, the extraction of the azimuthal and radial velocity was repeated at each sampling point to obtain a 3D distribution of the near-wellbore velocity.

2.5. Automatic extraction based on adaptive time window

Although the STC method improves the radial resolution by processing the grouped receiver waveforms, the large amount of data makes the calculation process time-consuming and unsuitable for the well-site environment. It can be observed that, as the group number increases, the average source distance z_k also increases, increasing the transmission paths of the refracted wave. The increase in the transmission time results in a right shift of the maximum correlation value of each mode wave in the STC image. To this end, we set an initial time window and let it move adaptively with the increase of the group number. We only calculate in the range of the time window each time so that it can be realized in real time by significantly reducing the amount of calculation.

For STC methods in well-site application, the time window width is typically determined by using the first arrival time of the target wave mode (e.g., refracted compressional wave) at the nearest receiver and the termination time at the farthest receiver, which usually covers 2000 μs or more. In contrast, our proposed method only requires a time window covering the waveform packet width of the target wave mode, and the width of the time window is about 600 μs, the slowness range of the traversal mode wave sets the ordinate, reducing the computational load in time-domain searching by 70%. The time span Δt of the window moving from one group to another can be approximated from the ray-tracing theory as:

$$\Delta t = \frac{d}{v_n} \tag{11}$$

where v_n is the velocity of the nth group, and d is the receiver spacing. The tracking of the target mode wave using Eq. (4) is shown in Fig. 6.

2.6. Velocity interpolation imaging

Actually, the 3D velocity profile obtained through the pre-processing is the superposition of 2D profiles in multiple azimuths. which is not easy to be observed and analyzed directly due to the lack of completeness. To obtain the complete 3D space

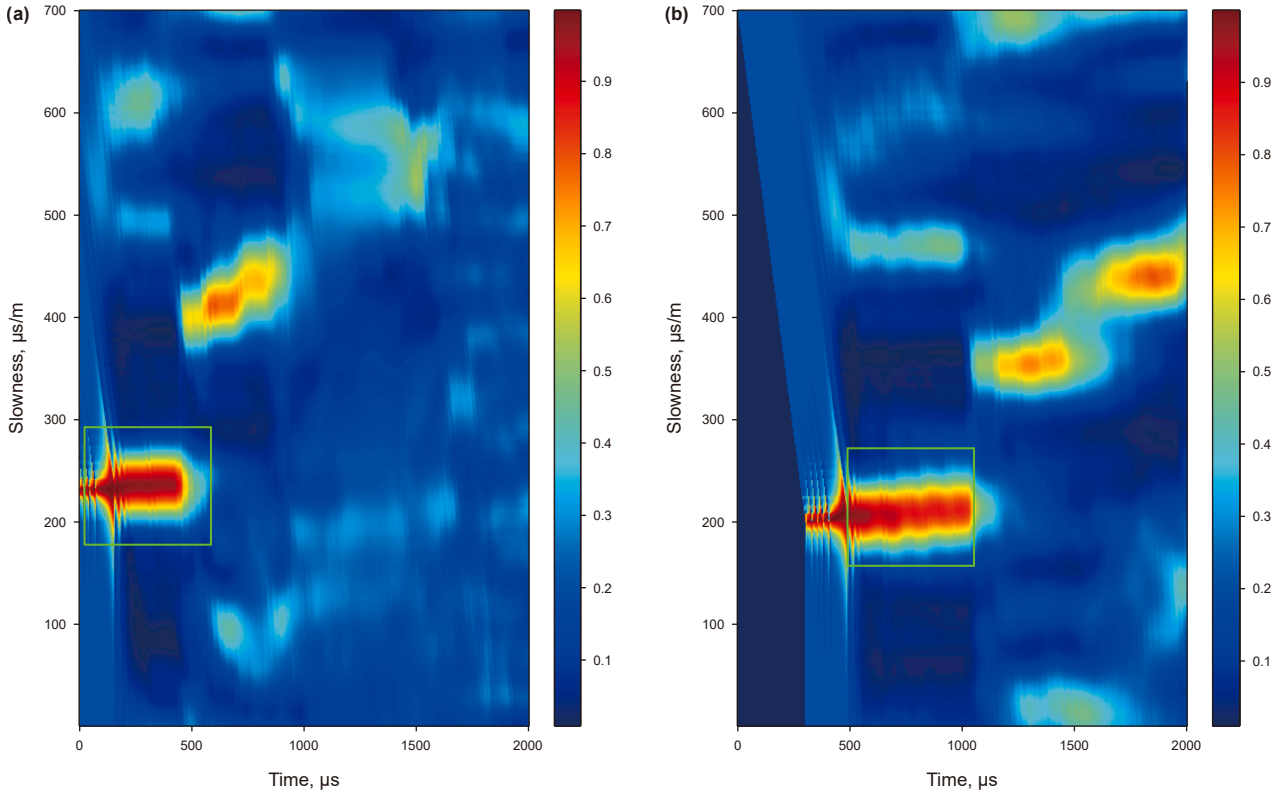

Fig. 6. Time window tracking results of different groups. **(a)** The first group of time window; **(b)** the last group of time window.

image, the interpolation method is used for the unsampled space. The IDW method is a commonly used deterministic model for spatial interpolation (Lu and Wong, 2008), and is popular among geoscientists because of its relative speed and ease of interpretation. It assumes that the attribute value of an unsampled point is the weighted average of known values within the neighborhood, and the weights are inversely related to the distances between the prediction location and the sampled locations. The inverse-distance weight is modified by a constant power or a distance-decay parameter to adjust the diminishing strength in a relationship with increasing distance. The discrete velocity value of the surrounding wellbore can be obtained. The IDW formulas are given as Eqs. (12) and (13):

$$\widehat{v}_p = \sum_{i}^{n} w_i v_i \tag{12}$$

$$w_i = \frac{d_i^{-\alpha}}{\sum_{i=1}^{n} d_i^{-\alpha}} \tag{13}$$

where $\widehat{v}_p$ means the unknown velocity value; v_i means the known velocity value through Eq. (6); n means the amount of velocity sequence; w_i means the weighting of each velocity sequence; d_i means the distance from each discrete velocity value to the unknown site; α means the power, and is also a control parameter, generally assumed as 2 (Zhu and Jia, 2004).

3. Numerical simulation

3.1. Model description

Our study uses the FDTD method to simulate the waveform with a grid size of 0.005 m. The formation model is a cylinder, whose bottom surface is a circle with a radius of 2 m, and the total height of the cylinder is 7 m. The cylinder is divided into eight identical regions at centre angle of 45-degree in the axial direction, and the eight receivers of the receiver ring are placed at the centre of the opening angle of these regions. The wellbore with a radius of 0.1 m was placed in the centre of the model, and the wellbore was filled with drilling fluid. The array acoustic logging instrument is placed in the centre of the wellbore, and the receiver rings are placed from (0 m, 0 m, 3 m) to (0 m, 0 m, 4.8288 m) with 0.1524 m spacing between adjacent receiver rings. Each receiver ring has eight azimuthal receivers, and the adjacent azimuthal receivers have an angle of 45° to receive signals from different azimuths. There are two transmitter positions, one at (0 m, 0 m, 2.6952 m) and the other at (0 m, 0 m, 0.7140 m), which simulate the lower-near monopole and far monopole sources. At each sampling point, two sound sources at different locations are excited separately, and waveforms are recorded at each azimuthal receiver for subsequent waveform reconstruction. A PML absorbing layer is set outside the formation model to absorb the boundary reflection signals due to the finite boundary and simulate the infinite formation in this way. A schematic of the formation model and the initial position of the logging instrument is shown in Fig. 7.

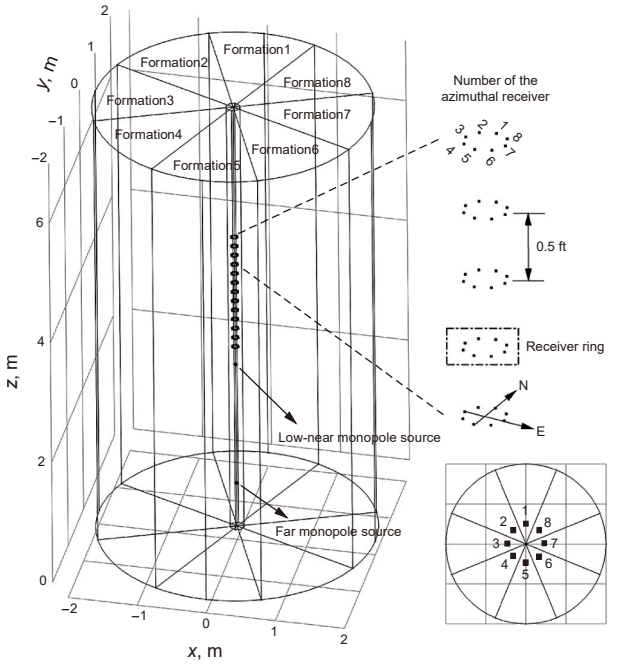

Fig. 7. The initial position of the instrument in the formation model and the description of the azimuthal receiver.

Table 1
Formation and fluid parameters.

Model	Density, kg/m^3	V_P, m/s	V_S, m/s
Borehole fluid	1000	1500	0
Formation 1	2160	2900	1900
Formation 2	2180	3200	2100
Formation 3	2200	3500	2300
Formation 4	2220	3800	2500
Formation 5	2240	4100	2700
Formation 6	2260	4400	2900
Formation 7	2280	4700	3100
Formation 8	2300	5000	3300

3.2. Wavefields in heterogeneous formations

3.2.1. Azimuthal heterogeneous formations

We first set formation parameters with different velocities and densities in the eight divided regions to simulate the situation of azimuthal heterogeneous formations around the well. Table 1 shows the eight formation parameters. Then, we excited the Ricker sound source at the location of the transmitters in the well, and the receiver recorded the sound pressure signal every 0.5 μs for 4.0 ms of logging response. In order to reveal the propagation law of acoustic waves in the azimuthal heterogeneous formation, we use the variable density map of acoustic pressure to show the propagation of acoustic waves in the formation model. Acoustic waves are affected by the heterogeneity and the spatial variation of the medium parameters in heterogeneous formations, and the response characteristics of wave field are complex and variable.

Fig. 8 shows the top view of the sound pressure of the refracted wave at the axial position of 3.0 m in eight moments. It can be seen that the refracted wave sound pressure first reaches the receiver 8 from the fastest stratum at 610 μs, and then reaches other receivers in order of formation speed from fastest to slowest, and reaches the receiver 1 at the slowest stratum speed at 925 μs. The inhomogeneity of formation can cause acoustic waves to be deflected and scattered in different directions and travel along multiple paths during propagation. This multipath propagation results in multiple arrival times and peaks in amplitude in the logging record, which makes it possible for the azimuthal receivers to record the wave field response in the wrong direction. Fig. 9 shows the waveform in the azimuth receivers at an axial position

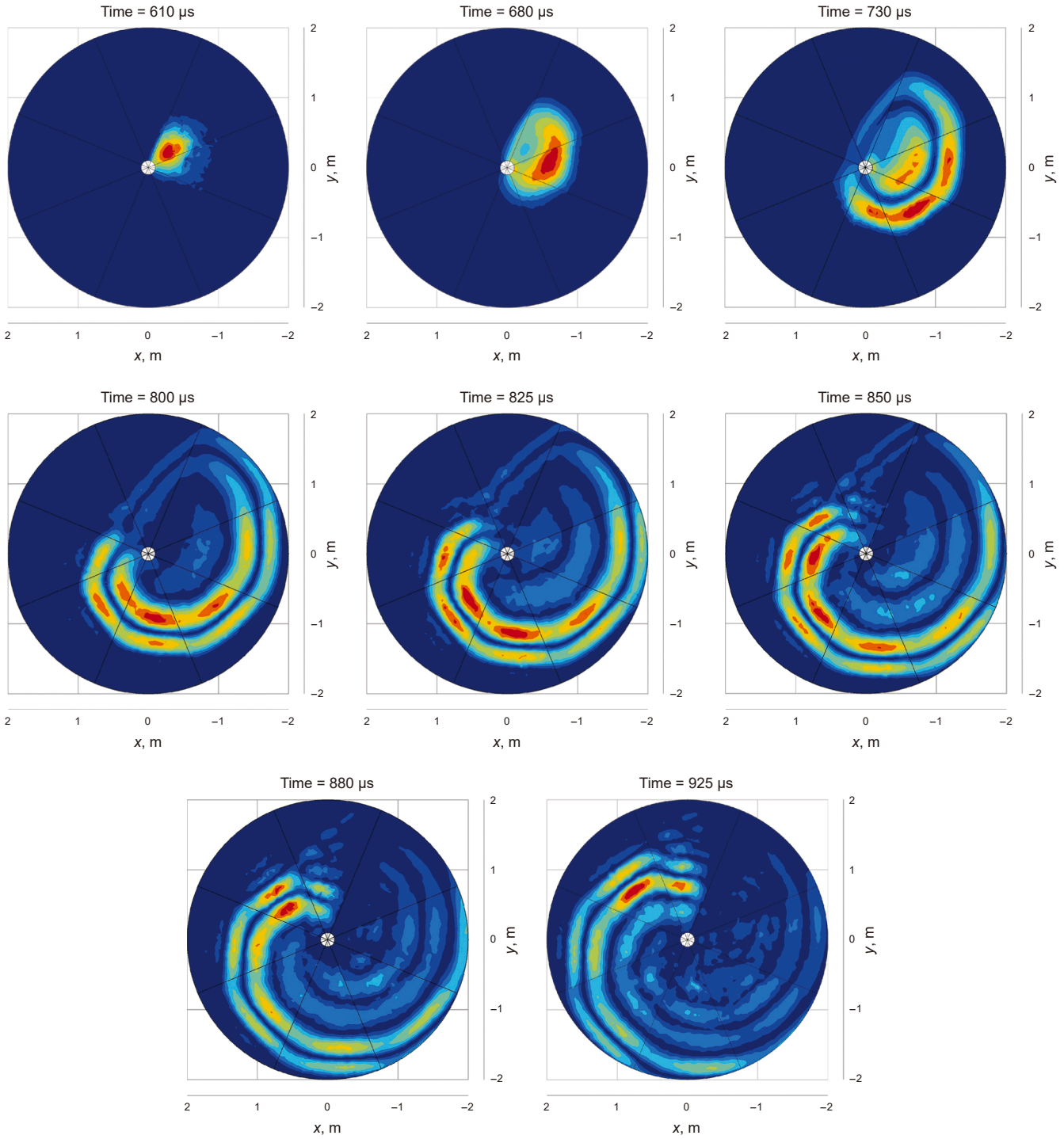

Fig. 8. The planar representation of the refracted wave's sound pressure at different moments (at the axial position of 3.0 m).

of 3.0 m, and we are unable to calculate the velocity by analyzing the arrival time of the first wave. To accurately obtain azimuthal velocity, it is necessary to apply bandpass filtering to the waveform of the receiver before extracting the azimuthal velocity.

3.2.2. Radial heterogeneous formations

During the drilling process, mechanical damage and fluid invasion affect the near-well formations, resulting in the refracted wave velocity of the near-wellbore formation being lower than that of the formation far away from the wellbore. Furthermore, the degree of this velocity change is typically inversely proportional to the radial distance between the formation and the wellbore. Therefore, based on the previous model, the azimuthal variation feature was removed, and five equally thick intrusion zones were introduced outside the wellbore. The radius of the wellbore remains 0.1 m, and each intrusion zone has a thickness of 0.2 m, while the thickness of the original formation is 0.9 m. The refracted wave velocities of the five intrusion zones, from farthest to nearest to the wellbore, are 95%, 90%, 85%, 80%, and 75% of the original formation refracted wave velocities. The planar

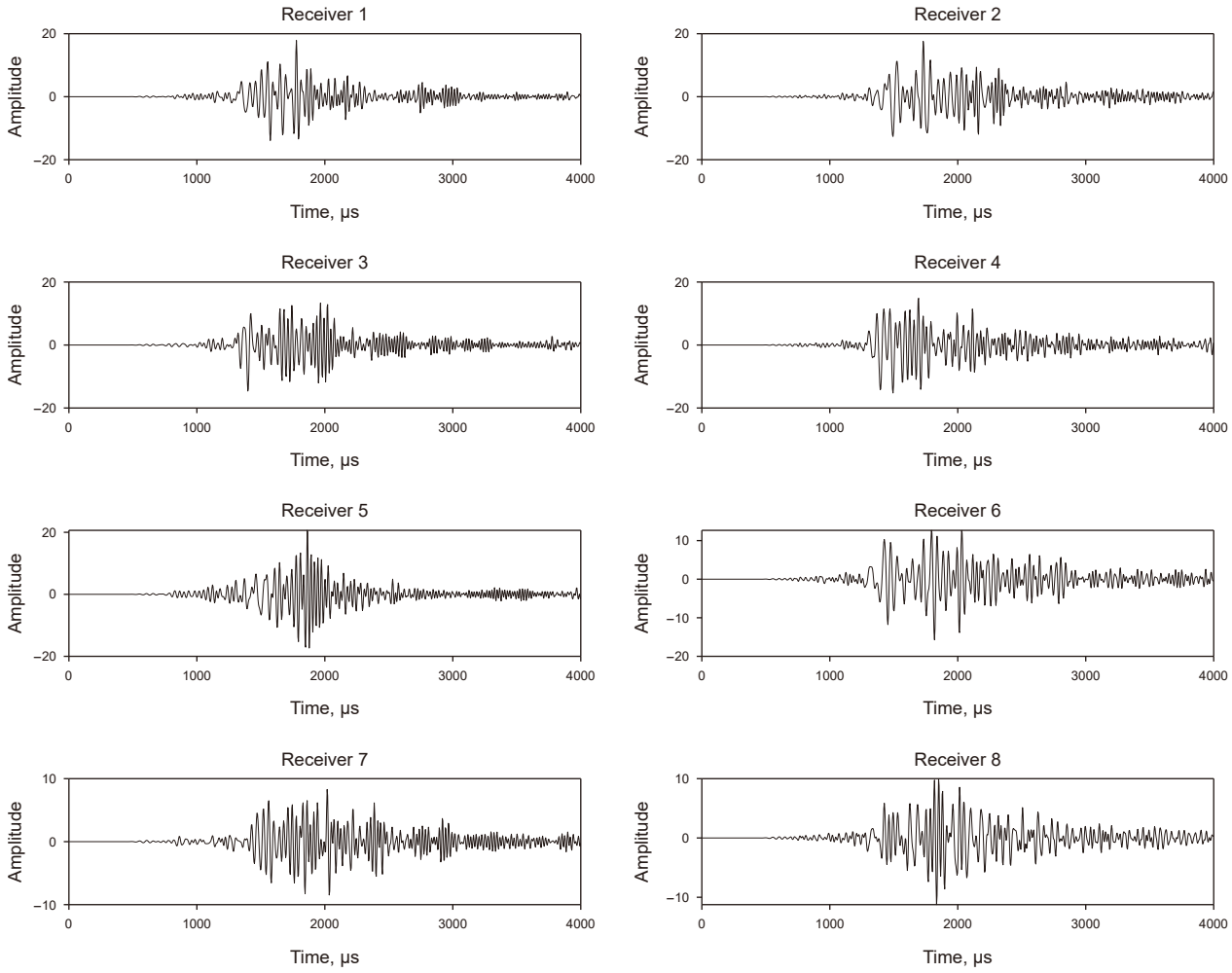

Fig. 9. The waveform in the azimuth receivers at the axial position of 3.0 m.

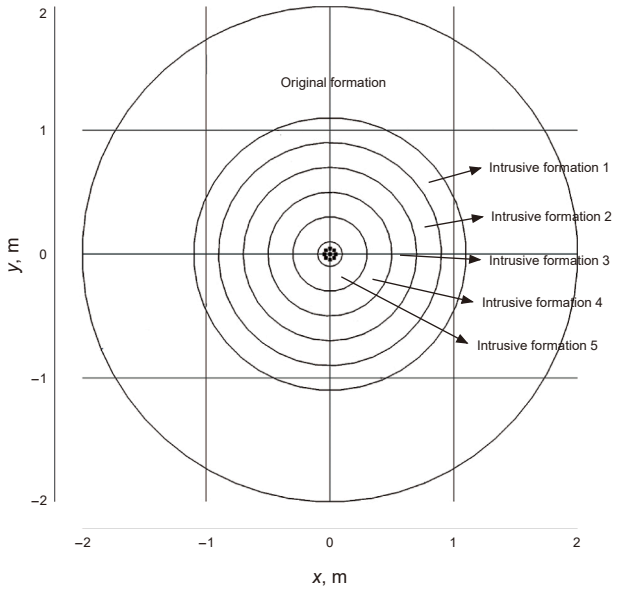

Fig. 10. The planar representation of the radial heterogeneous formation model.

Table 2
Formation and fluid parameters.

Model	Density, kg/m^3	V_P, m/s	V_S, m/s
Borehole fluid	1000	1500	0
Intrusive formation 1	2050	3750	2475
Intrusive formation 2	2100	4000	2640
Intrusive formation 3	2150	4250	2805
Intrusive formation 4	2200	4500	2970
Intrusive formation 5	2250	4750	3135
Original formation	2300	5000	3300

representation of the formation model is depicted in Fig. 10 and detailed parameters can be found in Table 2. The presence of intrusion zones results in refraction of the refracted compressional and shear waves between layers, as shown in Fig. 11. This interbeds refraction and slow near-well formations result in a delay in the arrival of the first wave signal. As the radial depth of detection increases with the offset, the delay time varies at different offsets. More significant arrival delays are observed at longer offsets. Compared to homogeneous formation, the waveforms of the heterogeneous formation model also display disparities in the amplitude of the refracted compressional wave, as can be seen in Fig. 12. However, changes in amplitude typically enable only a

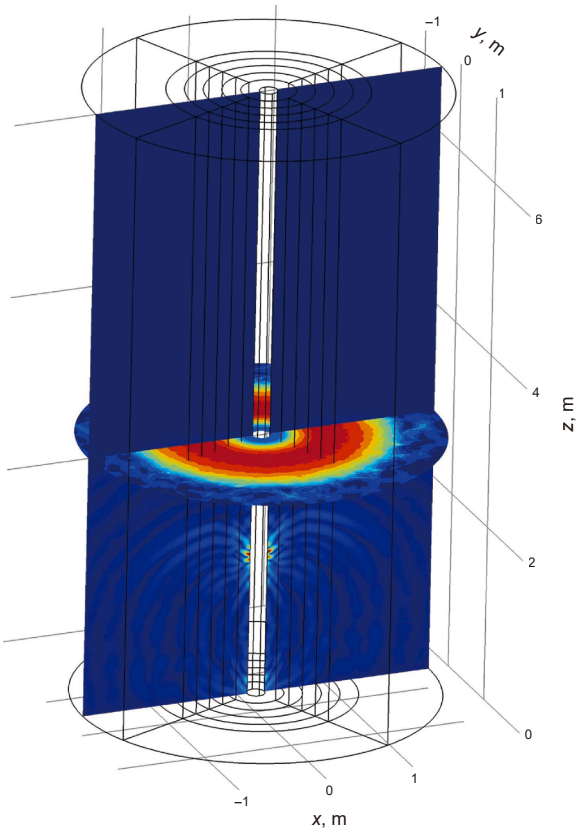

Fig. 11. The propagation characteristics of the wave field in radial heterogeneous formation.

qualitative assessment of the presence of intrusion formations near the wellbore. In this study, the velocity of radial heterogeneous formations is quantitatively determined based on discrepancies in the arrival times of refracted waves at varying source distances.

3.2.3. Azimuthal and radial heterogeneous formations

We considered a model which is more representative of actual subsurface conditions, as heterogeneity in formations typically involves both azimuthal and radial variations. Thus, based on the formation model shown in Fig. 7, we added five intrusion formations as shown in Fig. 13. We initially populated eight layers with different properties in eight directions, as detailed in Table 1. Subsequently, within a 1-m thickness between radial distances of 0.1 m–1.1 m, we added five intrusion formations at equal intervals, with each layer being 0.2 m thick. The velocity characteristics of these five intrusion formations are consistent with those described in the previous section on radial heterogeneous formations. The azimuthal and radial heterogeneous formation model simultaneously exhibits the characteristics of radial heterogeneous formations and that of azimuthal heterogeneous formations. Due to the azimuthal heterogeneity of the formation model, the refracted wave sound pressure propagates first from the fast formation, and then to the slow formation. Additionally, due to the radial heterogeneity, the propagation of the refracted waves is affected by the deceleration in the intrusion formations and interbed refraction. Fig. 14(a) and (b) show the difference in the refracted wave sound pressure between the formations of azimuthal and radial heterogeneity and the formations of only azimuthal heterogeneity.

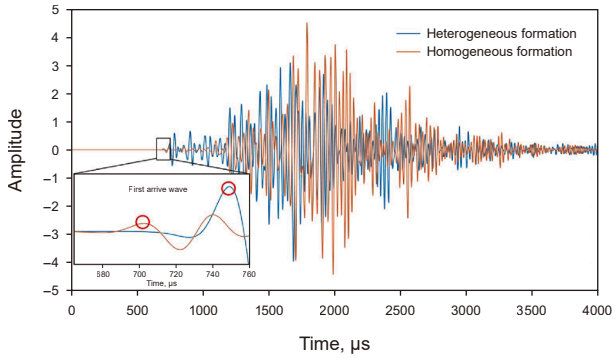

Fig. 12. Waveform differences between homogeneous and heterogeneous formation models.

It can be observed that at the same axial position, the intrusion results in a delayed arrival of the refracted wave. Therefore, for this complex situation, we need to use filtering methods first to avoid azimuthal interference, and then use the STC method to extract velocity sequences at different source distances. Combining the velocity sequences in each direction using the Eqs. (8)–(10), we can invert the velocity sequences into velocity distributions, ultimately construct the velocity distributions in multiple directions. Verifying the accuracy of the inversion is also a concern, thus, the next section will focus on validating the accuracy of this method.

3.3. Accuracy verification

3.3.1. Azimuthal accuracy verification

To obtain the starting and ending frequency values for the bandpass filter, we use the WSS method to separately process the refracted compressional and refracted shear waves in array acoustic logging in azimuthally heterogeneous formations, in order to determine their predominant frequency range. This section mainly focuses on refracted compressional waves, and the treatment for refracted shear waves is similar, hence it is not further elaborated. Fig. 15 shows the results of the WSS method processing for refracted compressional waves in eight azimuths. It can be observed that different azimuths result in different predominant frequency ranges for the refracted compressional waves, leading to different frequency lower and upper limits (f_1 and f_2) for the bandpass filtering. For instance, the f_1 of receiver 1 should be selected as 12181.5 Hz while f_2 should be chosen as 16943.4 Hz. Upon establishing the specific frequency ranges required for each azimuth, we applied bandpass filtering to the original well-logging waveforms according to the Eqs. (4) and (5), and the images before and after filtering are displayed in Fig. 16(a). We used Eq. (6) to extract the refracted compressional wave velocities from the datasets before and after filtering. Prior to filtering, the impact of scattering energy makes it impossible to distinguish changes in the formation velocities based on direction, therefore, the image primarily displayed the result of the fastest formation 8. By employing the filtration method we proposed, this issue has been effectively addressed, which is evident from the results obtained from the receivers in different directions. From receiver 1 to receiver 8, the extracted velocity values are continuously increasing, consistent with the assumptions made in our initial formation model. Fig. 16(b) and (c) effectively demonstrate the impact of filtering on the results. Fig. 16(d) presents the azimuthal velocity extraction results, the azimuthal velocity extraction results after filtering have accurately reflected the formation model,

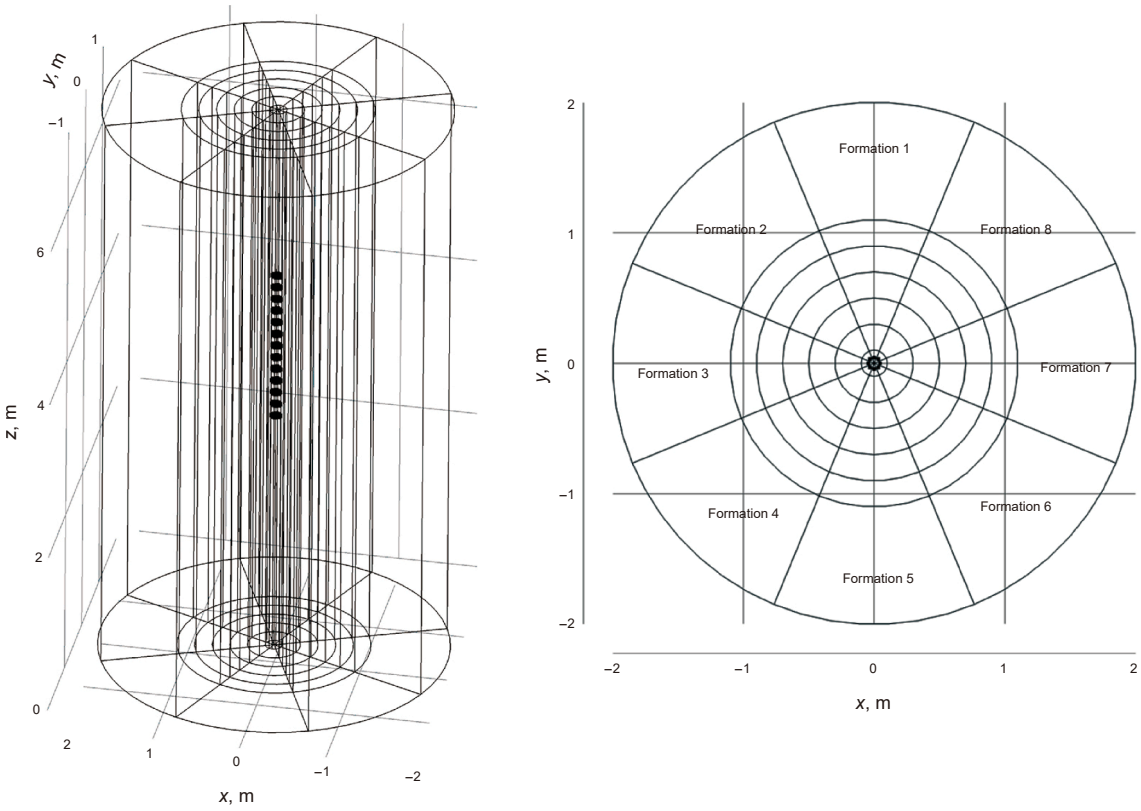

Fig. 13. The formation model with simultaneous azimuthal and radial heterogeneity characteristics.

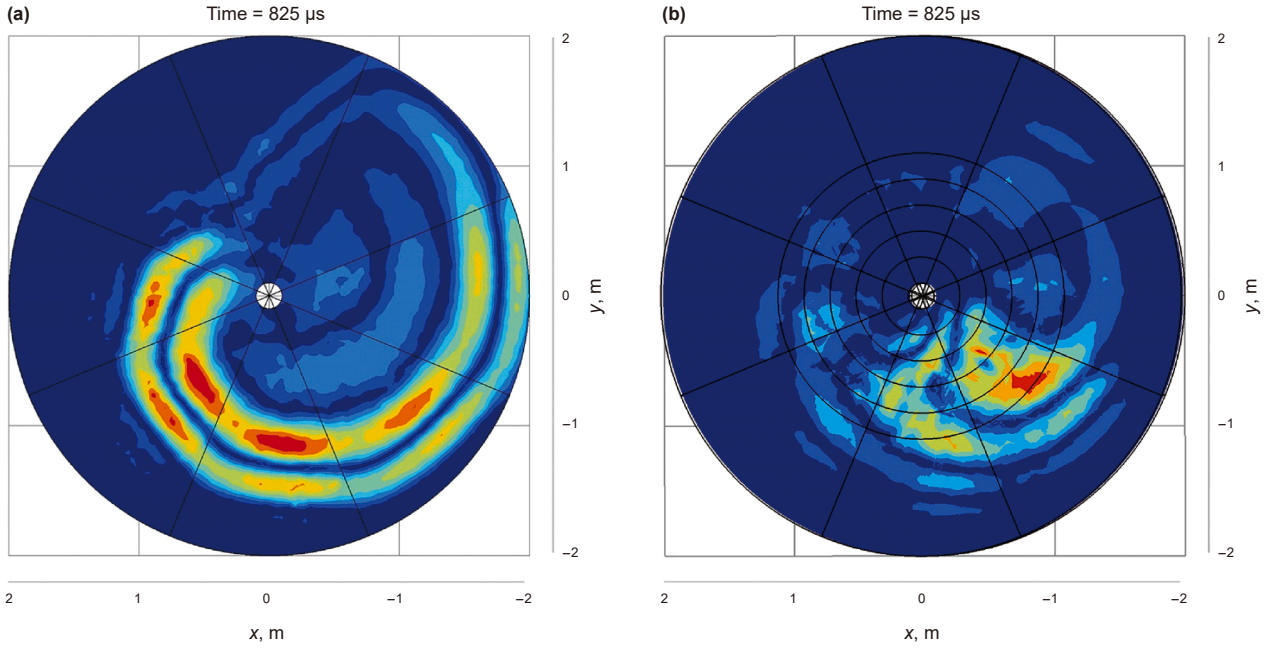

Fig. 14. The difference in the refracted wave's sound pressure between only azimuthal heterogeneous formations and azimuthal and radial heterogeneous formations (at the axial position of 3.0 m). **(a)** Only azimuthal heterogeneous formations; **(b)** azimuthal and radial heterogeneous formations.

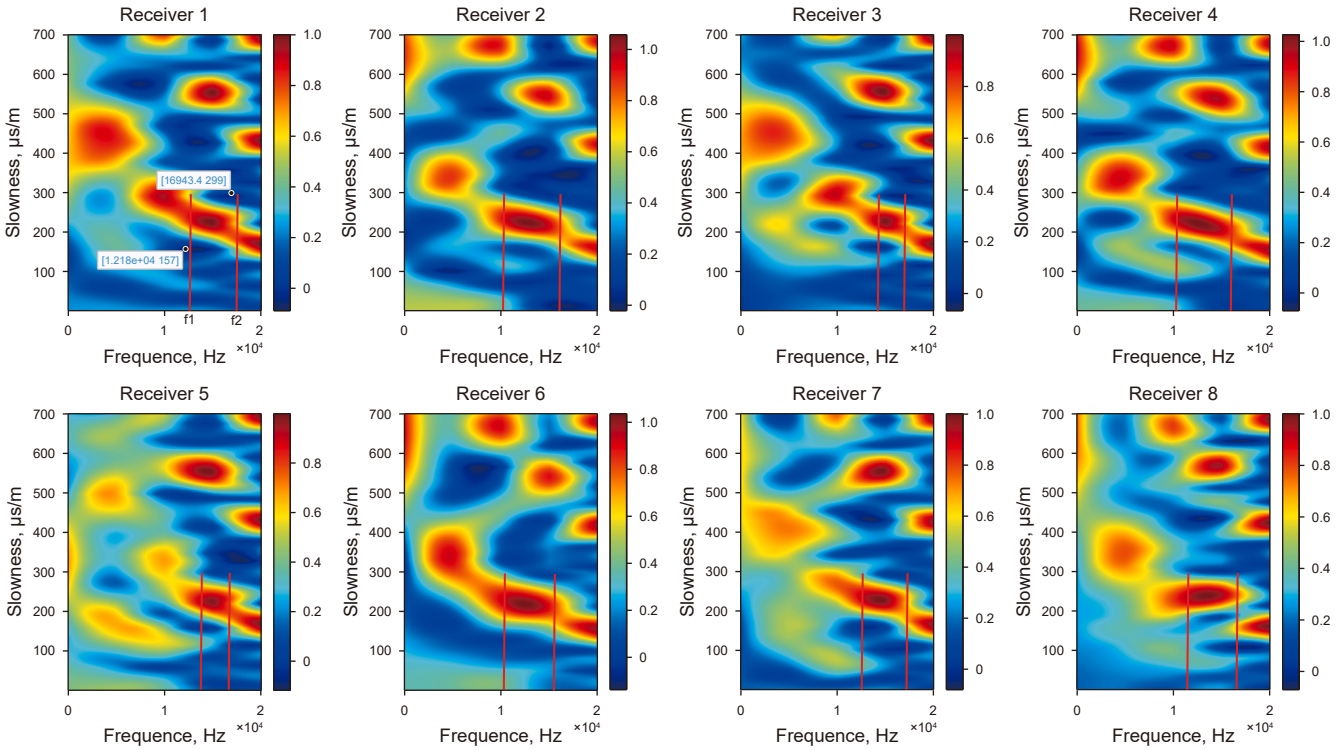

Fig. 15. Determine the frequency band for band-pass filtering in 8 directions with the WSS method.

demonstrating the effectiveness and accuracy of the azimuthal velocity extraction method.

3.3.2. Radial accuracy verification

To obtain the radial distribution of formation velocity, we initially need to extract the refracted wave velocities for each group using the STC method, thereby forming a velocity sequence for a depth point. Then we use this velocity sequence as the input in Eq. (8) to ultimately obtain the velocity profile at that depth point. We grouped the combined single-shot 26 receiver data sets, performing three velocity extractions using groups of 4, 5, and 6 receivers, respectively, and demonstrated the results of radial refracted shear wave velocity extraction under different grouping conditions (the steps for extracting the refracted compressional wave sequence are the same), as shown in Fig. 17. Based on the results, as the number of receivers in each group increases, the radial resolution decreases, specifically reflected in the increase in errors between the first velocity sequence and the refracted shear wave velocity of intrusive layer 1. This is because, with an increase in the number of receivers, the average source distance for each group also increases, resulting in a loss of near-well formation information. However, if the number of receivers in each group is too low, the correlation of the STC method also decreases, leading to an inaccurate extraction of velocity. Therefore, within the scope of the method usage, minimizing the number of receivers in each group is advantageous for the accuracy of radial velocity imaging. We use the velocity sequences of 4 receivers per group as inputs for Eqs. (8)–(10) to obtain the corresponding layer thickness H_n for each velocity sequence. On this basis, we apply Eqs. (12) and (13) for interpolated imaging to enhance continuity. A comparison between the velocity inversion profile and the original formation model is shown in Fig. 18. At a radial depth of 0.1 m, the inversion result is 2512 m/s, slightly higher than the refracted shear wave velocity of the first intrusive layer. At a radial depth of 1.1 m, the inversion result is 3263 m/s, slightly lower than the refracted shear wave velocity of the original formation. The overall error is less than 2%. Regarding intrusive thickness, the intrusion of the formation model extends up to 1.1 m, while the inversion result is 1.07 m. This confirms the radial accuracy of the proposed method.

3.3.3. Both azimuthal and radial accuracy verification

The previous two sections verified the accuracy of the inversion process for formation models with solely azimuthal and solely radial heterogeneity. In this section, we will verify whether the method can accurately invert the velocity distribution in a formation model containing both azimuthal and radial heterogeneity. First, we use Eqs. (3)–(6) to extract velocity sequences from the data of receivers in each direction, and then substitute them into Eqs. (7)–(10) to obtain the distribution of these velocity sequences in their respective directions. Repeating this process 8 times yields the velocity distribution for 8 directions, the velocity inversion results for 8 directions are shown in Fig. 19. The inversion results show that the obtained velocity near the well is consistently faster than the actual values. This is due to the detection range of array sonic logging tool is unable to accurately obtain information about the formation at a radial depth of 0.2 m. Regarding the zones far from the well, the inversion results are generally very close to the real situation. In addition, when azimuthal heterogeneity is high, the accuracy of the inversion results is lower than that of the formations with lower azimuthal heterogeneity. For example, in Fig. 19(a) and (h), corresponding to the velocity distribution of formation 8 and formation 1, the inversion results are heavily influenced by the nearby formations due to the significant difference in refracted wave velocities between these two formations. Overall, the proposed method can effectively and accurately invert the velocity of formations with simultaneous azimuthal and radial heterogeneity.

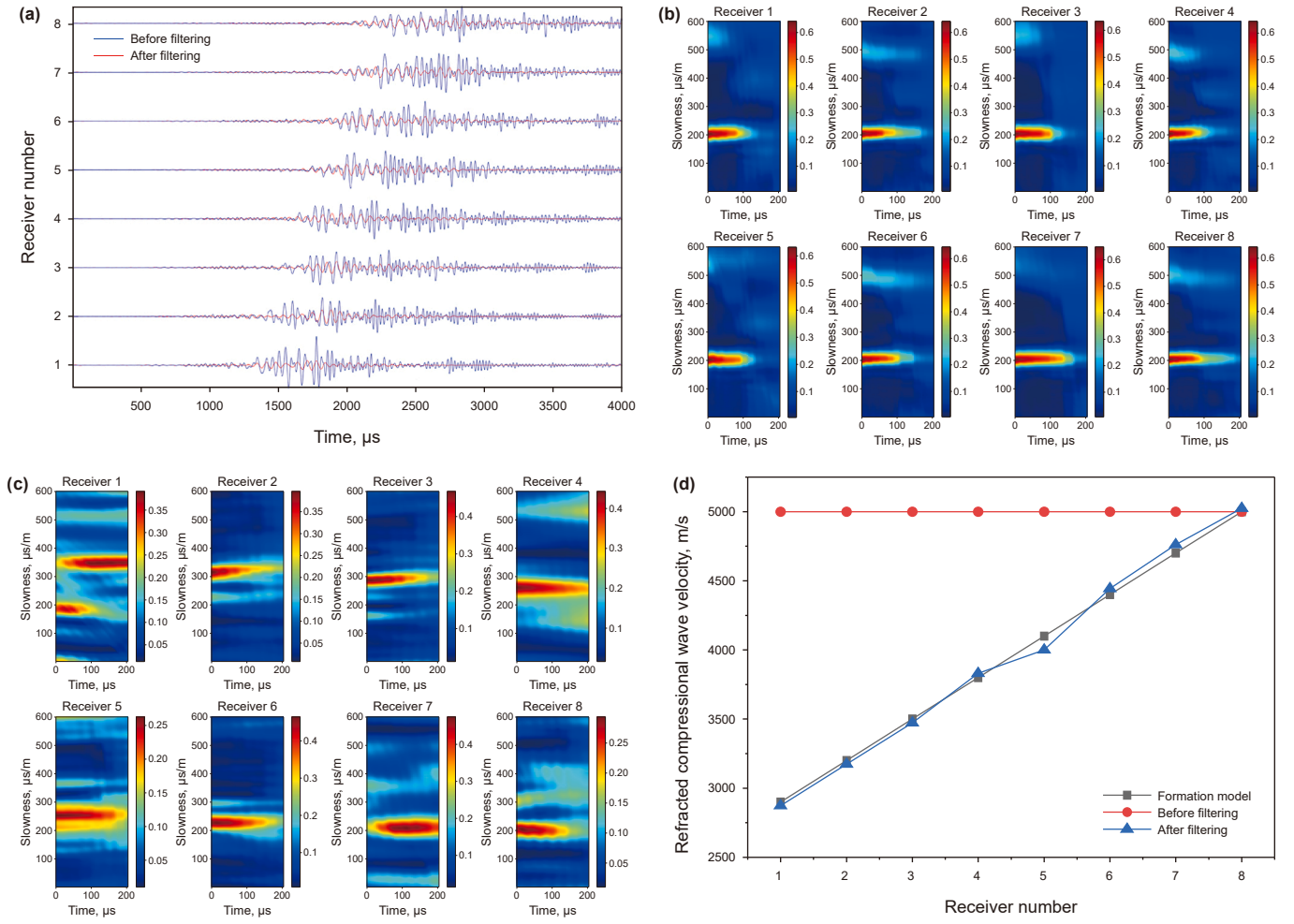

Fig. 16. Verification of the accuracy of azimuthal velocity distribution. **(a)** The waveform results before and after filtering; **(b)** the velocity extraction results in 8 directions before filtering; **(c)** the velocity extraction results in 8 directions after filtering; **(d)** the comparison results with the formation model.

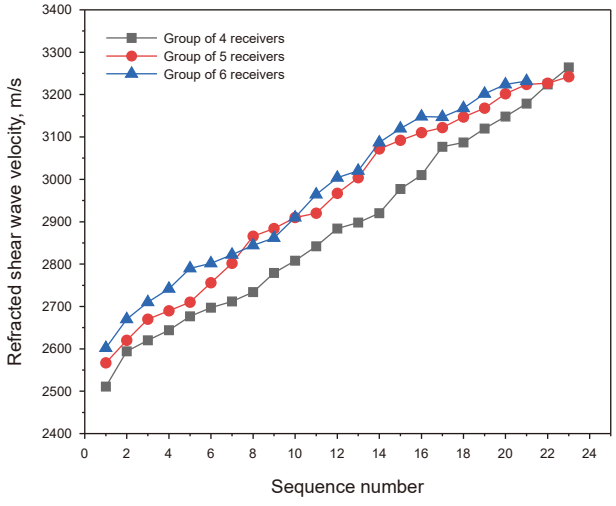

Fig. 17. Results of velocity sequence extraction with different numbers of receivers.

4. Field example

We can obtain accurate formation anisotropy parameters from dipole acoustic logging data, which can identify fractures, design hydraulic fracturing, and directional perforating schemes, and determine borehole stress. However, Due to the vectorial nature of flexural wave, whose polarization orientation exhibits axial symmetry in physical terms, the measurement cannot distinguish between the true direction and its antipodal direction. This inherent limitation manifests in the anisotropy profile as two solutions separated by 180°. This inherent ambiguity precludes unambiguous determination of the principal anisotropy direction, leaving a 180° directional uncertainty unresolved by the current measurement paradigm. Fig. 20 presents a field example study from western China using XMAC logging data acquired with 8 receivers (4 azimuthal components per receiver). The four azimuthal compressional wave velocity profiles resolve the inherent 180° ambiguity of dipole shear-wave anisotropy measurements, enabling unambiguous determination of the principal anisotropy orientation. In Fig. 20, panel 1 and panel 2 show the gamma-ray (GR) logging curves and depth scale for the 20 m formation interval. Panel 3 shows a dipole shear-wave waveform in the time domain of 0–4000 μs, including the waveforms of fast and slow shear waves respectively. Panel 4 shows the slowness of the fast and slow shear waves obtained from the inversion of the dipole shear waveform shown in panel 3, and the orange area represents the separation of the fast and slow shear waves. Panel 5 shows the anisotropy results obtained from panel 4 inversion, ANI and ANIA logging curves are the array anisotropy and its average results. Panels 6–9 show the results of compressional wave

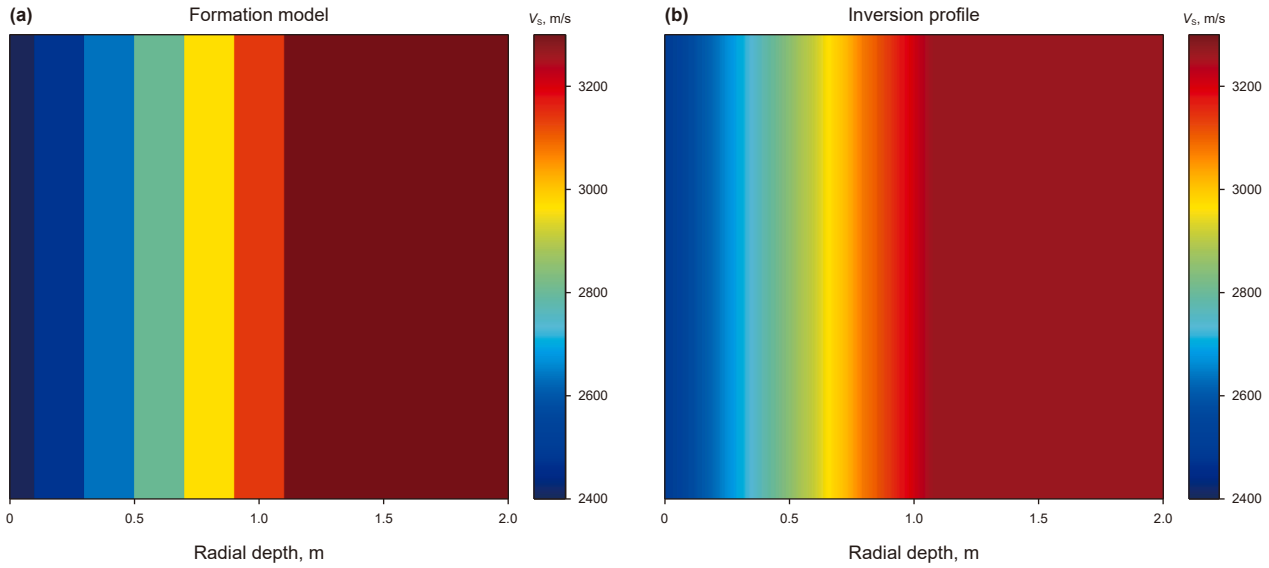

Fig. 18. Verification of the accuracy of the radial velocity distribution. **(a)** Formation model; **(b)** inversion profile.

velocity profile in four directions based on the near-wellbore 3D velocity imaging method proposed in this paper. Panel 10 displays the dipole shear-wave anisotropy profile, with 0° representing north.

Panel 3 reveals distinct shear wave splitting phenomena within the studied depth interval, characterized by the separation of fast and slow shear waves, which qualitatively demonstrates the presence of formation anisotropy. Panels 4 and 5 reveal the magnitude of this anisotropy has been quantitatively determined based on the time delay between fast and slow shear wave arrivals, enabling the identification of five anisotropic ranges within the formation. Through the lateral comparison of panels 6–10, it can be seen that the dipole shear-wave anisotropy results have good correspondence with the results of the compressional wave velocity, and the proposed method not only provides radial velocity information missing from traditional methods but also determines the specific azimuthal orientation of anisotropy. Within the depth from 2135.2 to 2138.5 m, panel 5 demonstrates strong dipole shear wave anisotropy while panel 10's anisotropy profile indicates principal orientations at 10° and 190° (N-S trend). The azimuthal compressional wave velocity results show that the velocity in the southern direction is higher than in the other three directions, confirming that the anisotropy in this depth interval is primarily caused by the southern 190° direction. Within the depths 2140.6–2141.8 m and 2143.8–2145.6 m, panel 5 demonstrates weaker dipole shear wave anisotropy while panel 10's anisotropy profile indicates principal orientations at 50° and 230° (NE-SW trend). The azimuthal compressional wave velocity results reveal that the velocity in the eastern direction is the lowest while the northern direction shows the highest values, demonstrating that the anisotropy within these two depth intervals is predominantly induced by the northeastern 50° orientation. Within the depth from 2147.5 to 2148.8 m, panel 5 demonstrates medium-strength dipole shear wave anisotropy while panel 10's anisotropy profile indicates principal orientations at 5° and 195° (N-S trend). The azimuthal compressional wave velocity results show that the velocity in the northern direction is higher than in the other three directions, confirming that the anisotropy in this depth interval is primarily caused by the northern 5° direction. Within the depth from 2151.0 to 2152.6 m, panel 5 demonstrates medium-strength anisotropy dipole shear wave anisotropy while Panel 10's anisotropy profile indicates principal orientations at 36° and 216° (NE-SW trend). The azimuthal compressional wave velocity results show that the velocity in the eastern direction is the lowest while the northern direction shows the highest values, demonstrating that the anisotropy in this depth interval is predominantly induced by the northeastern 36° orientation. By analyzing the velocity profile results of panels 6–9, it can be seen that the formation velocity at a radial depth of less than 0.2 m is lower than that at a distance from borehole, which is due to the varying degrees of decrease in near-borehole velocity caused by drilling fluid intrusion. This field example confirms that the proposed method agrees well with dipole shear wave anisotropy results, can obtain accurate three-dimensional velocity distribution from measured data, and can effectively characterize anisotropy directions through compressional wave velocity distribution results.

5. Conclusion

We propose a fast 3D velocity imaging method for array acoustic logging instruments equipped with azimuthal receivers, which can efficiently image the near-wellbore 3D velocity distribution. Through our proposed workflow, the array acoustic logging data can be inverted into a near-wellbore 3D velocity profile, thereby addressing the limitations of radial and azimuthal sensitivity in conventional methods. To verify the accuracy of the proposed method, we used the finite difference time domain (FDTD) numerical simulation to generate synthetic data. The results demonstrated the method's effectiveness in inverting velocity profiles in formations with azimuthal heterogeneity, radial heterogeneity, and combined heterogeneities. Additionally, the method has been applied to field data from array acoustic logging, and the inversion results were in good agreement with those obtained using conventional methods. The field example also showed that the proposed method can effectively determine the direction of anisotropy. It should be noted that the azimuthal resolution of this method depends on the receiver's azimuthal components, with the resolution being 360° divided by the number of receiver azimuthal components. Current logging tools typically have 4 or 8 azimuthal components, resulting in a minimum azimuthal resolution of 90° or 45° respectively. The identification accuracy of this method is limited when the azimuthal

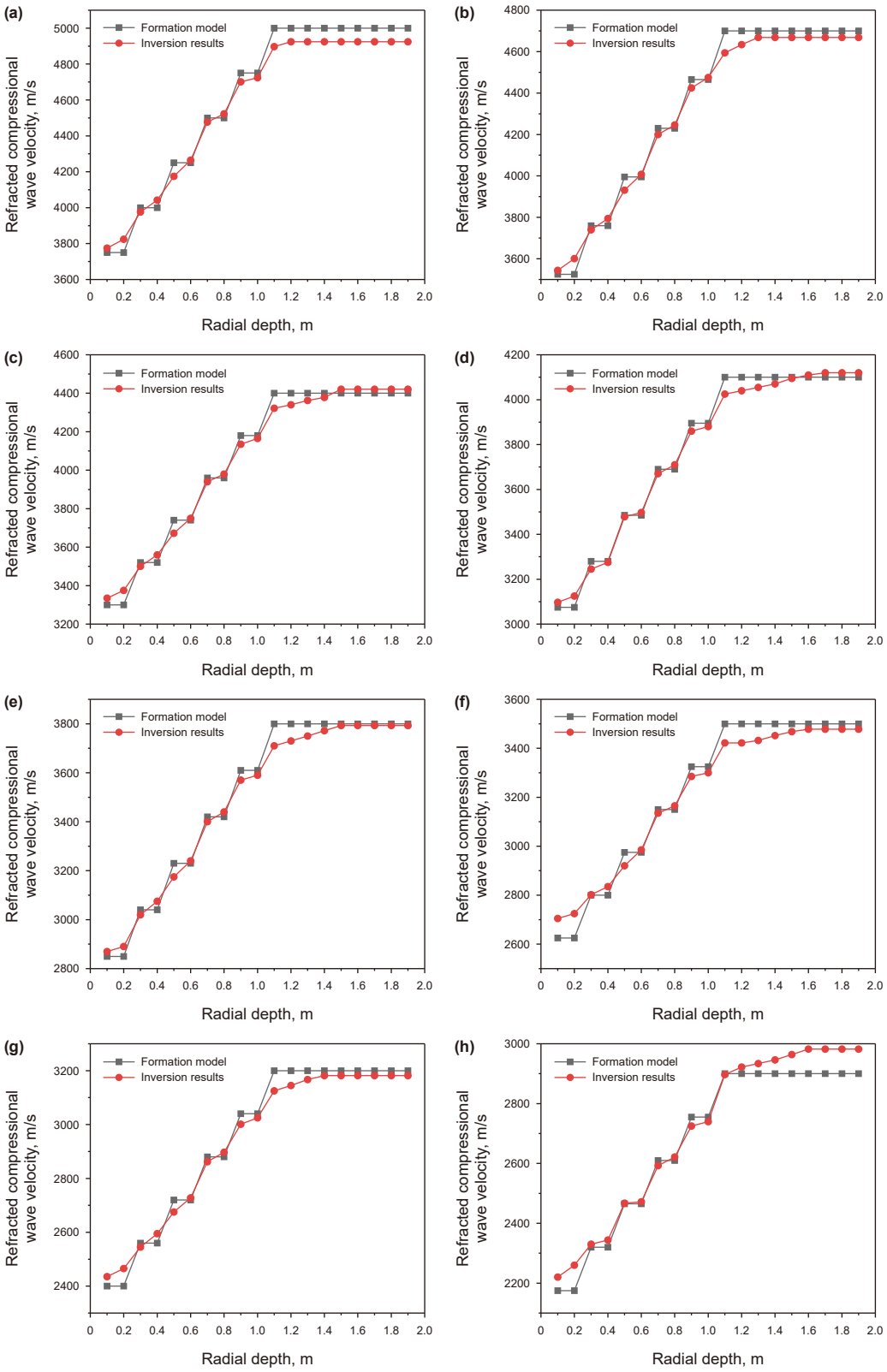

Fig. 19. The velocity distribution results in 8 directions. **(a)** The direction of receiver 8; **(b)** the direction of receiver 7; **(c)** the direction of receiver 6; **(d)** the direction of receiver 5; **(e)** the direction of receiver 4; **(f)** the direction of receiver 3; **(g)** the direction of receiver 2; **(h)** the direction of receiver 1.

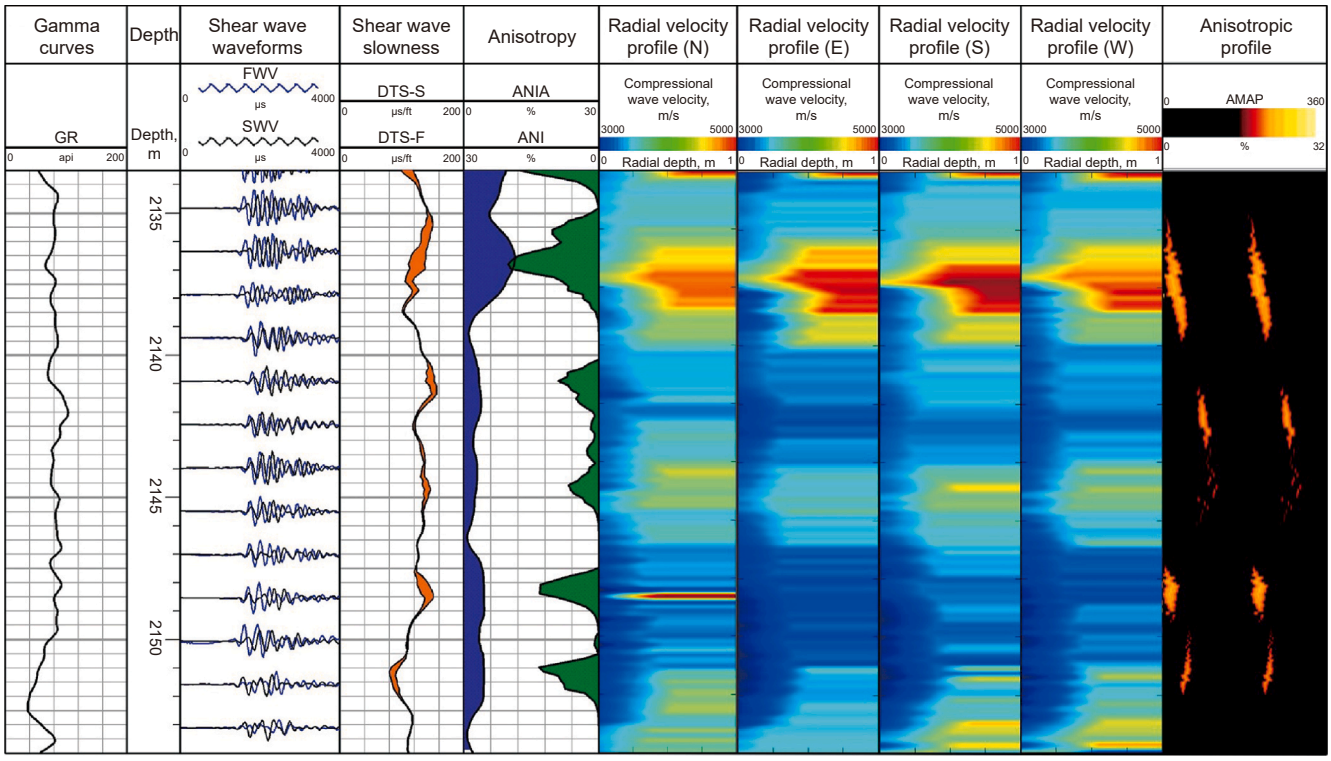

Fig. 20. Application of three-dimensional velocity profile in indicating anisotropic orientation.

variation range is smaller than the minimum resolution. Theoretically, as the number of the receiver's azimuthal components increases, the azimuthal resolution of this method can be further improved.

While this method shows great potential in unconventional reservoir exploration and development, particularly in hydraulic fracturing evaluation and near-wellbore mesh fracture evaluation, its limitation in azimuthal resolution should be considered when interpreting results in formations with small-scale heterogeneities. Future work may focus on improving the azimuthal resolution to enhance the method's ability to detect smaller structures.

CRediT authorship contribution statement

Zi Wang: Writing – original draft, Validation, Software, Formal analysis, Data curation, Conceptualization. **Wen-Zheng Yue:** Writing – review & editing, Visualization, Resources, Funding acquisition. **Yu-Ming Zhu:** Supervision, Resources, Project administration. **Nai-Xuan Ji:** Visualization. **Shan-Shan Fan:** Project administration.

Declaration of competing interest

The authors declare that they have no known competing financial interests or personal relationships that could have appeared to influence the work reported in this paper.

Acknowledgement

This research was financially supported by the National Natural Science Foundation of China (Grant Nos. 42174129 and 41374143) and the project of “Vice President of Science and Technology” of Changping District, Beijing (Grant No. 202502003019).

References

Backus, G., Gilbert, F., Bullard, E.C., 1970. Uniqueness in the inversion of inaccurate gross earth data. Phil. Trans. Roy. Soc. Lond. 26 (1173), 123–192. https://doi.org/10.1098/rsta.1970.0005.

Baker, L.J., Winbow, G.A., 1988. Multipole P-wave logging in formations altered by drilling. Geophysics 53 (9), 1207–1218. https://doi.org/10.1190/1.1442561.

Bourbié, T., Coussy, O., Zinszner, B., et al., 1992. Acoustics of Porous Media. Acoustical Society of America. https://doi.org/10.1121/1.402899.

Cheng, N., Cheng, C.H., Toksöz, M.N., 1995. Borehole wave propagation in three dimensions. J. Acoust. Soc. Am. 97, 3483–3493. https://doi.org/10.1121/1.412996.

Dines, K.A., Lytle, R.J., 1979. Computerized geophysical tomography. Proc. IEEE 67 (7), 1065–1073. https://doi.org/10.1109/PROC.1979.11390.

Hornby, B.E., 1997. Tomographic reconstruction of near-borehole slowness using refracted borehole sonic arrivals. Geophysics 58 (12), 1726–1738. https://doi.org/10.1190/1.1443387.

Kimball, C.V., Marzetta, T.L., 1984. Semblance processing of borehole acoustic array data. Geophysics 49 (3), 274–281. https://doi.org/10.1190/1.1441659.

Lei, H., Hei, C., Luo, M.Z., et al., 2019. The effects of near well heterogeneities on single-well imaging: numerical studies. Waves Random Complex Media 31, 1378–1395. https://doi.org/10.1080/17455030.2019.1663958.

Liu, Y., Chen, H., Li, C., et al., 2021. Radial profiling of near-borehole formation velocities by a stepwise inversion of acoustic well logging data. J. Petrol. Sci. Eng. 196, 107648. https://doi.org/10.1016/j.petrol.2020.107648.

Lu, G.Y., Wong, D.W., 2008. An adaptive inverse-distance weighting spatial interpolation technique. Comput. Geosci. 34 (9), 1044–1055. https://doi.org/10.1016/j.cageo.2007.07.010.

Ma, M.M., Chen, H., He, X., et al., 2013. The inversion of shear wave slowness's radial variations based on the dipole flexural mode dispersion. Chin. J. Geophys. 56, 2077–2087. https://doi.org/10.6038/cig2013062.

Nolte, B., Rao, R., Huang, X.J, 1997. Dispersion analysis of split flexural waves. Massachusetts Institute of Technology.

Pistre, V., Kinoshita, T., Endo, T., et al., 2005. A modular wireline sonic tool for measurements of 3d (azimuthal, radial, and axial) formation acoustic properties. In: SPWLA 46th Annual Logging Symposium.

Sayers, C.M., Adachi, J., Taleghani, A.D., 2008. The effect of near-wellbore yield on elastic wave velocities in sandstones. In: SEG Technical Program Expanded Abstracts, pp. 339–343. https://doi.org/10.1190/1.3054818.

Schisselé, E., Guilbert, J., Gaffet, S., et al., 2004. Accurate time-frequency-wavenumber analysis to study coda waves. Geophys. J. Int. 158, 577–591. https://doi.org/10.1111/j.1365-246X.2004.02211.x.

Sinha, B.K., 2004. Near-wellbore characterization using radial profiles of shear slownesses. In: SEG Technical Program Expanded Abstracts, pp. 326–329. https://doi.org/10.1190/1.1851270.

Sinha, B.K., Vissapragada, B., Kisra, S., et al., 2005. Optimal well completions using radial profiling of formation shear slownesses. In: SPE Technical Conference & Exhibition. https://doi.org/10.2118/95837-MS.
Sinha, B.K., Vissapragada, B., Renlie, L., Tysse, S., 2006. Radial profiling of the three formation shear moduli and its application to well completions. Geophysics 71, E65–E77. https://doi.org/10.1190/1.2335879.
Tarantola, A., 1984. Inversion of seismic reflection data in the acoustic approximation. Geophysics 49, 1259–1266. https://doi.org/10.1190/1.1441754.
Tang, X.M., Li, Z., Hei, C., et al., 2016a. Elastic wave scattering to characterize heterogeneities in the borehole environment. Geophys. J. Int. 205, 594–603. https://doi.org/10.1093/gjiw037.
Tang, X.M., Xu, S., Zhuang, C.X., et al., 2016b. Quantitative evaluation of rock brittleness and fracability based on elastic-wave velocity variation around borehole. Petrol. Explor. Dev. 43 (3), 457–464. https://doi.org/10.1016/S1876-3804(16)30053-2.
Tang, H.G., Cheng, A.C.H., Li, Y.E., et al., 2023. Borehole acoustic full-waveform inversion. Geophysics 88 (4), D271–D293. https://doi.org/10.1190/geo2021-0741.1.
Valero, H.P., Tejada, M., Murray, D., 2004. Improved first-motion algorithm to compute high-resolution sonic log. In: SPE Annual Technical Conference and Exhibition. https://doi.org/10.2118/90995-MS.
Wang, Z., Yue, W., 2024. An inversion method for imaging near-wellbore thin beds slowness based on array acoustic logging data. Front. Earth Sci. 12, 1292561. https://doi.org/10.3389/feart.2024.1292561.
Walker, K., Granville, J., Kainer, G., et al., 2015. Logging services: towards the 3D measurement of formation properties in high-resolution with a continuous depth of investigation. In: SPE Annual Technical Conference and Exhibition. https://doi.org/10.2118/175093-MS.
Willis, M.E., Toksöz, M.N., 1983. Automatic P and S velocity determination from full waveform digital acoustic logs. Geophysics 48, 1631–1644. https://doi.org/10.1190/1.1441444.
Winkler, K.W., 2005. Borehole damage indicator from stress-induced velocity variations. Geophysics 70 (1), F11–F16. https://doi.org/10.1190/1.1852772.
Zeroug, S., Valero, H.P., Bose, S., et al., 2006. Monopole radial profiling of compressional slowness. In: SEG Technical Program Expanded Abstracts, pp. 354–358.
Zhu, H.Y., Jia, S.F., 2004. Uncertainty in the spatial interpolation of rainfall data. Prog. Geogr. 23, 34–42. https://doi.org/10.11820/dlxjz.2004.02.005.